

# HIGH-ORDER ACCURATE RECONSTRUCTION SCHEME FOR THE RAYLEIGH-TAYLOR AND RICHTMYER-MESHKOV INSTABILITIES USING ARBITRARY UNSTRUCTURED MESHES

Pericles S. Farmakis, Panagiotis Tsoutsanis

Centre for Computational Engineering Sciences, Cranfield University, Cranfield MK430AL, UK  
[pericles.farmakis@cranfield.ac.uk](mailto:pericles.farmakis@cranfield.ac.uk), [panagiotis.tsoutsanis@cranfield.ac.uk](mailto:panagiotis.tsoutsanis@cranfield.ac.uk)

## ABSTRACT

A suite of computational experiments for the two-dimensional compressible Euler equations using a weighted essentially non-oscillatory (WENO) finite volume scheme is presented, investigating the effects of a state-of-art unstructured solver on the development of the Rayleigh-Taylor (RTI), and Richtmyer-Meshkov (RMI) instabilities. High orders of accuracy (up to the sixth-order) are attained as a result of polynomial reconstructions within the WENO framework, and the HLLC and Rusanov fluxes, coupled with three different, unstructured meshing algorithms are employed for the RTI. Two triads of cases for the RMI use conserved and characteristic variables, varying the central stencil weight size in the process. The effects of the numerics, the gravitational acceleration and shock-waves on the evolution of the two instabilities are displayed and contrasted. It is observed that the meshing algorithms affect the symmetry of the forming structures irrespective of resolution and numerical scheme; the characteristic variables resolve the flow features better, and HLLC is more accurate.

**Keywords:** iLES, WENO, unstructured mesh, RTI, RMI, KHI, Reynolds number, shock-waves, shock-tube, Riemann problem, HLLC, Rusanov flux, Astrophysics, ICF.

## 1. INTRODUCTION

The scope of this article is to probe large-scale turbulent mixing by applying certain conditions which trigger the Rayleigh-Taylor (see Taylor (1950)), Richtmyer-Meshkov (see Richtmyer (1960)) instabilities and their secondary companions (see for example Vorobieff et. al., 2004 [1]). The two are oftentimes working together to drive the flow, and accurately resolving the flow structures of instability-driven flows is of paramount importance in astrophysics, explaining f.e. the evolution of the intricate structures between gas layers observed in supernova remnants, or planetary nebulae, all of which seed their surrounding interstellar medium with vitalising heavy elements Zhou et. al., 2017 [5]. In human scale, said instabilities are entangled with geological activity and affect the atmospheric weather patterns, they can be beneficial in the industry by amplified mixing in mixing chambers and scramjet combustors. In some fundamental applications, they can be very disruptive and thus very much undesirable.

One such instance is the release of energy by inertial confinement fusion (ICF), Kull, 1991 [1]. During inertial confinement of a thermonuclear “target”, the aforementioned instabilities spawn from asymmetric irradiation of the target, and become aggravated by minuscule manufacturing imperfections of the surface of the target, or by any adjacent structure that breaks the **geometric** symmetry of the target, like the filling tube. The RT- and RM-driven flows undergo linear and non-

linear evolution, and transiently transcend to turbulence. This earlier stage of development is followed by a later stage, where mixing occurs in an envelope. If not contained, RTI and RMI constitute an escalating probability of quenching the reaction in the target, introducing unacceptably high levels of mixing. The ensuing mixing is a malignant limitation to ICF's full use as a mode for a commercial energy generation platform.

Common denominator for all Rayleigh-Taylor and Richtmyer-Meshkov flows, is the existence of perturbations along fluid interfaces; the structures resulting from the Rayleigh-Taylor instability are rooted to the acceleration of the heavier of the two fluids into the other, while those developing from the Richtmyer-Meshkov instability, form explicitly by the interaction of shock-waves with dints along material interfaces Zhou (2017). The present work sets out to investigate such complicated flow structures and the effects whereupon of a high-order accurate, WENO-based iLES in-house solver, the UCNS3D, deploying, multiple meshing algorithms, the conserved and characteristic variables, and the HLLC, and the Rusanov Riemann solvers. The ongoing project is perhaps one of the first to investigate the effects of an unstructured solver in such detail. This work, one in a series prepared by the authors, breaks new ground in numerical development towards highly reliable solvers for the RTI and the RMI.

## 2. THE NUMERICAL EXPERIMENTS

### 2.1 The Rayleigh-Taylor Instability

#### 2.1.1 Initial Comments

A representative study of the Rayleigh-Taylor instability is the one of Zhang, Shu, and Zhou (2006) [5], using Cartesian meshes within the framework of the Navier-Stokes equations. The Reynolds number was assumed to be  $Re = 25,000$ . Their study is followed up with this work, with the simulation of the same RT unstable flow using unstructured meshes and the Euler equations. The Reynolds number assumed previously is merely indicative for this work, since the Euler equations are fundamentally inviscid; an effective numerical Reynolds number does exist due to the nature of iLES, but if the numerical viscosity could be accounted for, the numerical Reynolds number would probably be smaller than the effective Reynolds number predicted from the Navier-Stokes.

Some sources of numerical viscosity in LES are the mesh (resolution, number of cell sides, both depending upon meshing algorithms), truncation errors, the (e.g. upwinding) bias of the numerical scheme due to sub-optimal stencil sizes, and (except for iLES) the explicit sub-grid scale model (SGS) for sizes under the cut-off wavenumber  $\kappa$ . The numerical viscosity accumulates, and the effective Reynolds number represents both this and the physical viscosity predicted by the Navier-Stokes equations. From Zhang, Shi, Shu, and Zhou (2003) [41], the Reynolds number dictates the complexity of the shape of the spike. Even with the Euler equations, increasing the mesh size (quantified by the  $x$ -axis mesh point number  $h$  below) and/or the order of accuracy of the scheme, the flow structures captured by the numerical solver correspond to larger *numerical* Reynolds numbers. Both the 2003 and the 2006 papers mentioned use the same basic numerical set-up, and the reader is referred to the article for more information.

The single-mode RTI investigated here is a rather unique type of flow. Its setup uses a sinusoidal perturbation in order to investigate the major structures forming *in isolation*, which is an idealized case. In ICF, incoherencies of the radiation field engendered by laser arrays add a "background noise" which leads to the formation of higher frequency, multimode RTIs in superposition with the longer wavelength perturbation of interest. Such noise is symmetry-breaking even from the start, making the

study of individual spikes and bubbles difficult. For simplicity, only one velocity perturbation is added along the fluid interface. Hence, at late times, minute irregularities solely from the numerical scheme and the mesh employed will grow and break the symmetry of the initial conditions. While no explicit symmetry-breaking terms to emulate are used in the setup, the idealized case has still physical value in ICF; such longer wavelength perturbations arise due to inherent radiation asymmetry modes akin to the Legendre polynomial P2 and P4 modes of the flux on an ICF capsule. Thus the present work shares the thinking of Zhou (2017), in which the asymptotic behavior of a single-mode RTI may prove good for investigating behaviors on regular surfaces found in experiments for the Euler equations.

### 2.1.2 The Numerical Test

The effects of the order of discretization and mesh size are made abundantly clear in the work of Zhang, Shi, Shu, and Zhou (2003), which defined (in a rather ad hoc manner) the required number of cells per wavelength (here denoted by  $h$ ), and how spatial resolution and polynomial degree in the WENO scheme result in different effective Reynolds numbers for the same setup. Subsequent work by Zhang, Shu, and Zhou (2006) simulated viscous RT flows for higher mesh resolutions, and, by extension, higher Re. In this work, two Riemann solvers are used; the HLLC (an upwind Riemann solver), and the Rusanov flux (a central scheme) in the original WENO scheme of Balsara and Shu (2000). The mesh sizes begun with  $h = 1/240$ , and refined to  $h = 1/480$ ,  $h = 1/960$  and  $h = 1/1920$  nodes. This number represents points on the boundary walls of the computational domain parallel to, or along the  $x$ -axis. The value is then multiplied by the domain's aspect ratio to assign nodes along the boundaries perpendicular to the  $x$ -axis. Results for the simulations of the latter mesh resolution are not yet available, and will be published separately in another publication. For the present study, the computational domain  $(x, y)$  extends to  $[0, 1/4] \times [0, 1]$  for the single-mode RTI. This was, in effect, the original size of the domain used by Zhang, Shi, Shu, and Zhou (2003).

The fluid-interface is located at  $y = 1/2$ . Above said interface, a light fluid having a density  $\rho = 1$  is suspended over a higher-density fluid lying below the interface with  $\rho = 2$ , while the source term applies a gravitational field pointing acceleration towards the lighter fluid, i.e. upwards. Finally, a pressure field expresses gravity in the initial conditions using for piezometric height co-ordinate  $y$ ; this "head" expresses the differences in potential energy between the fluid strata.

$$I.C. = \begin{cases} (\rho, u, v, p) = (2.0, 0.0, -0.025c_s \cdot \cos(8\pi x), 2y + 1), & y \leq 0.5, \\ (\rho, u, v, p) = (1.0, 0.0, -0.025c_s \cdot \cos(8\pi x), y + \frac{3}{2}), & y > 0.5. \end{cases} \quad (1)$$

The density contours for each simulation were plotted at physical times  $T = 1.85; 1.9; 2.1; 2.3$  and  $2.5$ , following the work of Zhang, Shi, Shu, and Zhou (2003) for consistency during post-processing and analysis. The order of accuracy varied from the WENO3 to the WENO6.

### 2.1.3 Results for the 2-D RTI

The results were studied using the density contours, the passive scalar, and vorticity fields. The two aforementioned fields provided a more complete understanding of how the pace of transition to turbulence is affected by meshing. From the analysis, one important observation, supported by the work of work by Zhang, Shu, and Zhou (2006), is that the symmetry of the initial conditions along the  $x$ -axis breaks eventually after the physical instability fully develops. This is observed in many

simulated RT-unstable flows, and is attributable to both numerical instabilities (e.g. due to entropy disparities, or the numerical Kelvin-Helmholtz instability), and their interaction with the physical instabilities. The latter becomes the dominant driving mechanism only with sufficient mesh resolution.

The evolution of the instability from the initially resting interface up to physical time  $T = 1.95\text{s}$ , using different Riemann solvers, mesh refinements and mesh algorithms, is presented in the following Figures. Because of the opposing pressure and density gradient, the initially linear RTI experiences exponential growth, with the heavy fluid intruding the lighter fluid, and the latter forming bubbles into the former. The flow patterns are similar; however the less diffusive HLLC starts to depart from symmetry and forms rather complex structures, full of vortex filaments “trailing” the ascending mushroom-cap. These secondary vortical movements instigate strong mixing of the lighter and heavier fluids. The overall motion apparently follows a specific way of evolution. The differences in momentum due to the density variation, forces the sinusoidal perturbation to form a mixing-layer.

This mixing layer promptly creates the well known structures of the KHI, which is rapidly strain due to shear of the two mixing fluids, one outside, and one inside the interface (towards the heavier fluid), and the latter is accompanied by additional such layers forming. Vortex pairing and roll-up ensue, and the 2-D simulations begin to diverge from actual flows, due to the inherent 3-D nature of these flows. Some streaks of heavy fluid are entrained within the lighter one. Mixing amplifies, and the heavy fluid displaces the lighter one to reach the domain’s upper wall, and reduce the PE of the system. With increased mesh refinement and order of discretization, smaller vortical structures and eddies merge due to the 2-D energy cascade into larger scales. Because strong non-linearity becomes more and more dominant, a large number of secondary roll-ups appear, particularly close to the cap; this is attributed to the KHI and secondary shear instabilities.

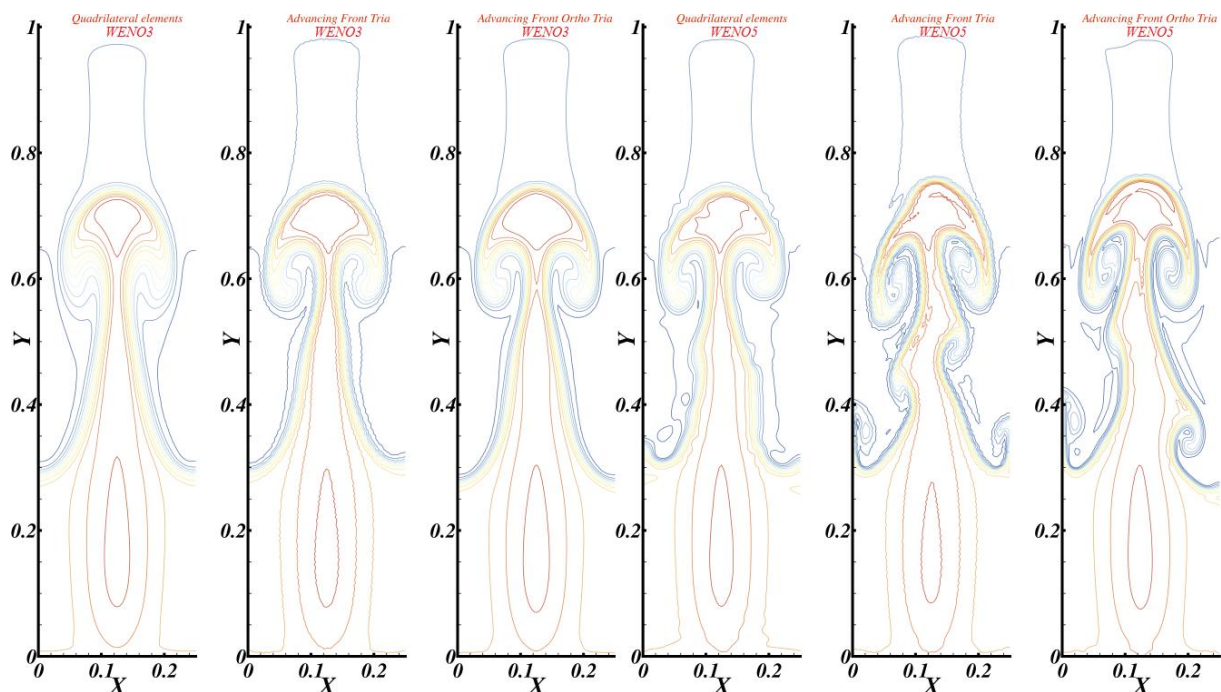


Figure 1. Contour density plots for the Rayleigh-Taylor instability at time 1.95s for the WENO3 (left) the WENO5 (right) schemes, and Rusanov’s flux. Mesh resolution is  $h = 1/240$ , and the meshing algorithms used are shown in red above each plot.

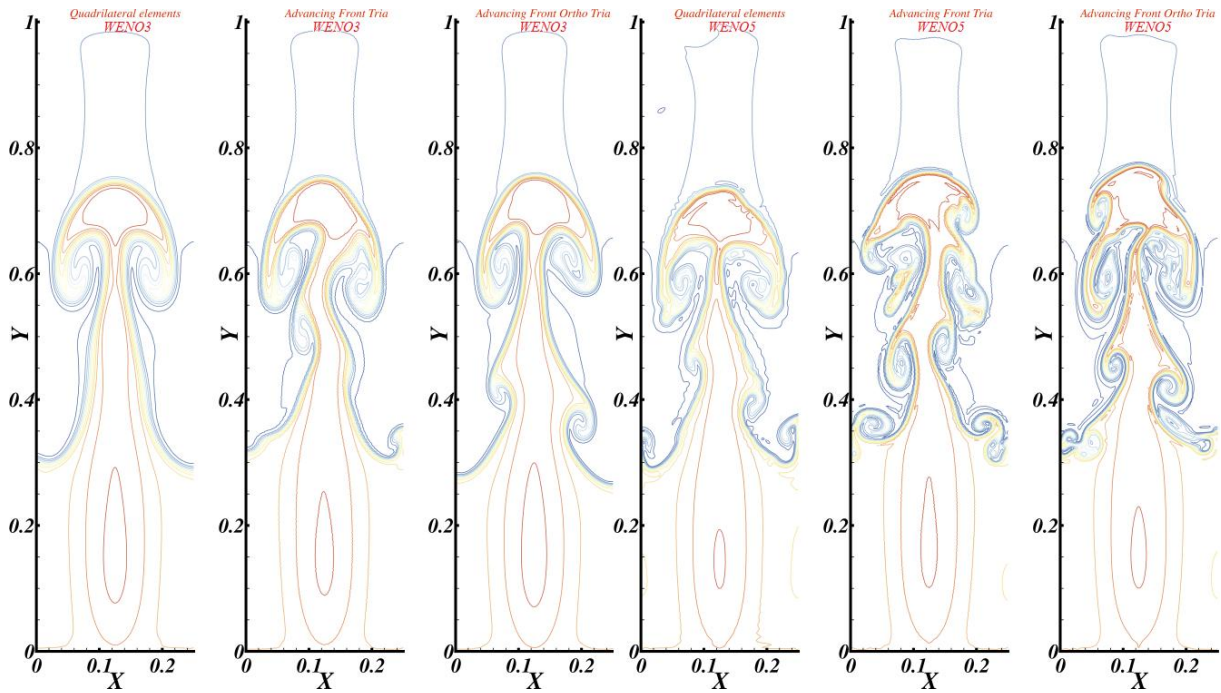


Figure 2. Contour density plots for the Rayleigh-Taylor instability at time 1.95s for the WENO3 (left) the WENO5 (right) schemes, and Rusanov's flux. Mesh resolution is  $h = 1/480$ , and the meshing algorithms used are shown in red above each plot.

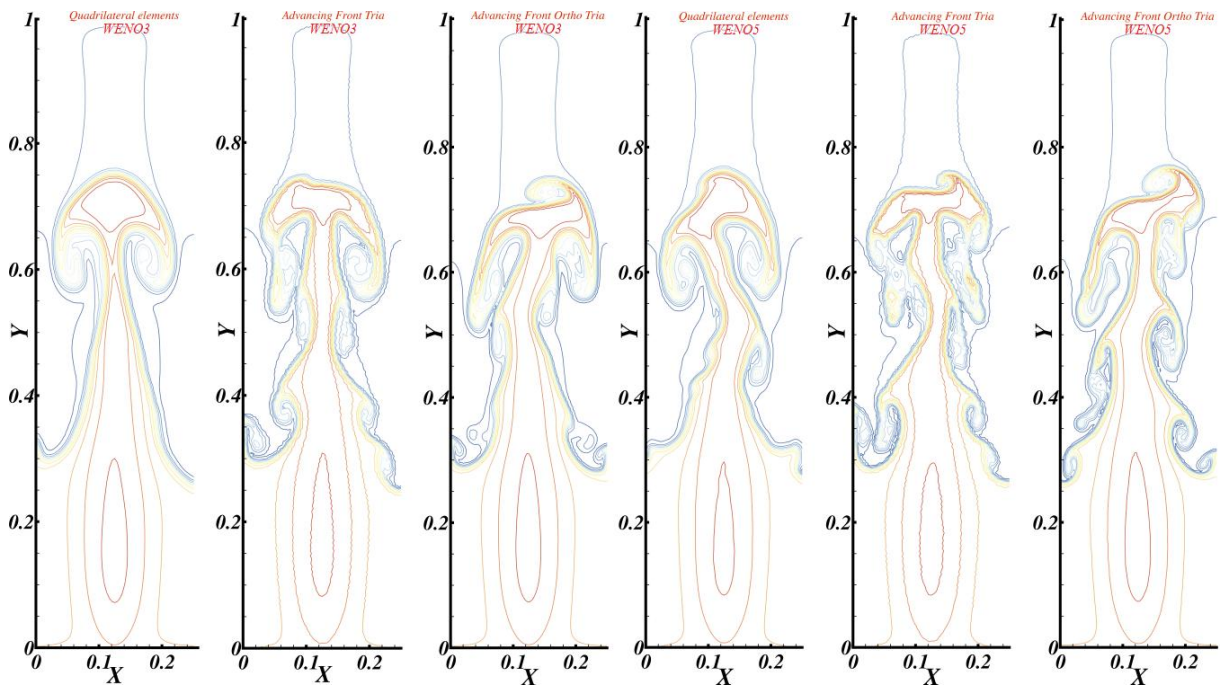


Figure 3. Contour density plots for the Rayleigh-Taylor instability at time 1.95s for the WENO3 (left) the WENO5 (right) schemes, and the HLLC flux. Mesh resolution is  $h = 1/240$ , and the meshing algorithms used are shown in red above each plot.

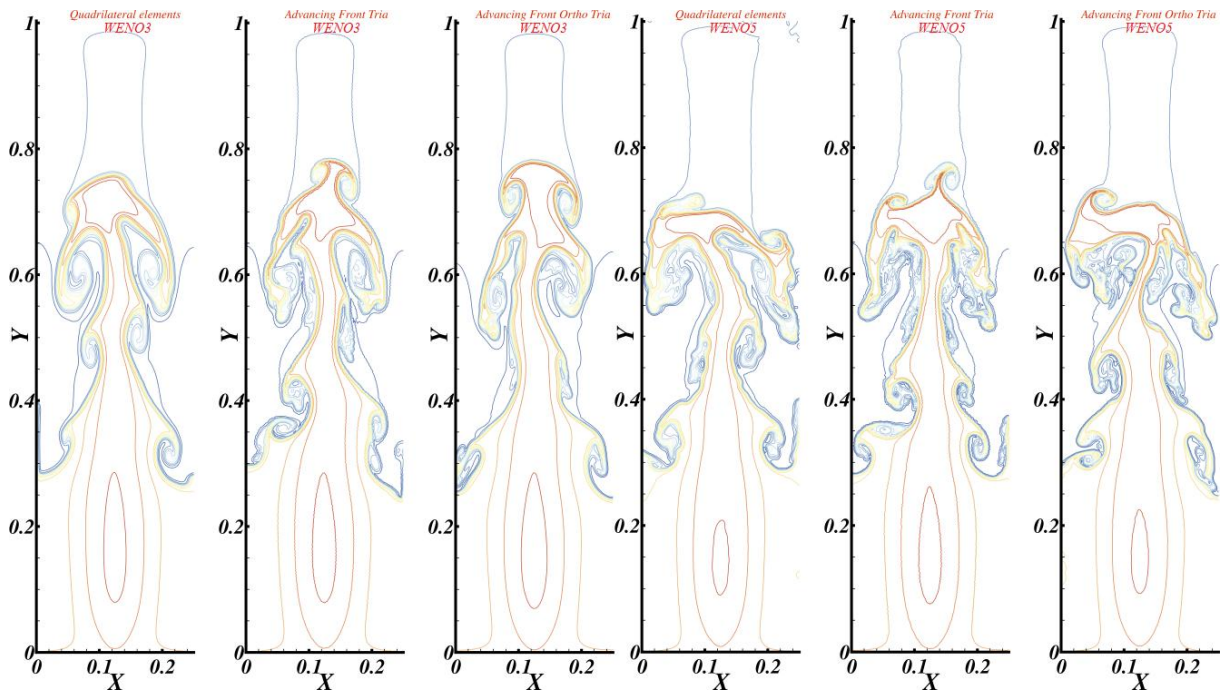


Figure 4. Contour density plots for the Rayleigh-Taylor instability at time 1.95s for the WENO3 (left) the WENO5 (right) schemes, and the HLLC flux. Mesh resolution is  $h = 1/480$ , and the meshing algorithms used are shown in red above each plot.

In Figures 1-4, the effects of the meshing algorithms are showed. Apparently, even by elevating the resolution, the algorithms have a decisive effect in the prediction of the forming structures. This is due to the workings of the algorithms which have a decisive impact to the way the stencils are formed based on them; the algorithms affect the grouping the cells as compactly as the algorithm permits each time, and also interfere with the stencil consistency and their less than optimum size. The number of edges in each element is also important, as it dictates the dissipation introduced by each finite volume. Thus the smaller the dissipation, and the more compact the stencil, the more easily a scheme for a given order of discretization will detect early the numerical instabilities that will drive the symmetry breaking for lower mesh resolutions.

On the other hand, due to the numerical KHI, which becomes more and more evident in higher resolutions, this numerical nuisance will boost the effects of the physical instabilities which dominate the drive of the flow with mesh refinements. At the same time, higher order of spatial accuracy also switches the flow according to the work of Zhang, Shi, Shu, and Zhou (2003) to higher effective (here numerical) Reynolds numbers, which impacts the shape and size of the RTI “fingers.”

## 2.2 The Richtmyer-Meshkov Instability

### 2.2.1 Opening Remarks

From the available work published in the open literature, the numerical set-ups for computational problems dealing solely with the Richtmyer-Meshkov instability are typically in the form of a classical shock-tube; a highly pressurized gas mixes through an interface with another gas of different density. This kind of perturbed interface is encountered in ICF, due to both surface roughness which manifests as rapidly growing in amplitude very high frequency symmetry breaking “noise.” The surfaces of a

target also demonstrate repetitive perturbations due to machining imperfections, in the form of regular (or periodic) dints or grooves. In shock-tube experiments, air has been used both with a light noble gas (f.e. helium), and with heavier polyatomic gases like sulfur hexafluoride ( $SF_6$ ) or acetone, see for example the work of Tritschler et. al. (2014). This material interface is simulated in 2D by a sinusoidal function in the density field.

### 2.2.2 The Numerical Case

One classical example for the RMI is provided by Zhang and Wang (2013) [73], for investigating WENO implementations and variations thereof. The boundary conditions are neither explicitly specified nor implied, though it is possible to infer them from related computational configurations found in the literature, which examine the instability in question; the shock-tube configuration is commonly encountered. Reflective boundary conditions are regularly used at the end-wall of the tube, and translational periodic for the lateral sides, while imposed or velocity inlet boundaries are used in the post-shock region. Imposed conditions are preferred for this work since velocity inlets routinely introduce severe starting errors when a shock is initialized in their proximity.

The initial conditions (I.C.) of Zhang and Wang (2013) (derived from the Rankine-Hugoniot relations) are for a 2-D shock-tube containing air and helium; the finalized domain used in this work measures  $[0, 6] \times [0, 1]$  at  $(x, y)$  to permit reshock of the structures at late times. The two gases (air and helium) are emulated with the same adiabatic index, like in the RTI simulations. The initial conditions, the spatial arrangement of the shock front (moving at  $M = 2.0$ ) and the interface for the mode of the Richtmyer-Meshkov instability read:

$$I.C. = \begin{cases} \left( \frac{\rho}{\rho_0}, \frac{u}{u_0}, \frac{v}{v_0}, \frac{p}{p_0} \right) = (2.67, 1.48, 0, 4.5), & x < 0.2, \\ \left( \frac{\rho}{\rho_0}, \frac{u}{u_0}, \frac{v}{v_0}, \frac{p}{p_0} \right) = (1, 0, 0, 1), & x \leq 1.2 \pm 0.1 \cdot \cos(n\pi y), \\ \left( \frac{\rho}{\rho_0}, \frac{u}{u_0}, \frac{v}{v_0}, \frac{p}{p_0} \right) = (0.138, 0, 0, 1), & x > 1.2 \pm 0.1 \cdot \cos(n\pi y). \end{cases} \quad (2)$$

The shock front and the perturbed interface reside in the highly-pressurized air volume, on the left of the shock-tube. The interface cosine form varied by  $n = 2, 4, 6$ , for the single, double, and triple mode.

### 2.2.3 Results for the 2-D RMI

The 2D shock-tube has been investigated using the conserved and the characteristic variables, in an effort to detect discrepancies in the mathematical approach used in the numerics. The complex structures for the three modes like the late-time roll-up of the spikes were illustrated using the density gradient magnitude for simulated Schlieren imaging, and density contours levels at physical times  $T = 0.0; 0.3; 0.6; 1.0; 1.65$ , and  $2.25$  seconds. The simulations used the WENO3 and WENO5 schemes and the HLLC Riemann solver and unstructured, fully quadrilateral meshes generated by the Advancing Front Ortho algorithm; 480,000 cells ( $1201 \times 201$  nodes).

For a single spike, the structures forming are complex. As the incident shock passes through the density gradient it generates a transmitted shock-wave. The incident and reflected shock-waves

smooth out the curved transmitted shock, and form a microscopic Mach stem downstream the forming cap. The cap “pulsates” re-transmitting shock-waves downstream; it confines diffracted oblique shocks and emanates them upstream, enriching the internal structures of the spike. Occasionally, these collaborate with reflected oblique shocks as the interface advances within the domain. Such interactions launch expansion fans trailing the interface.

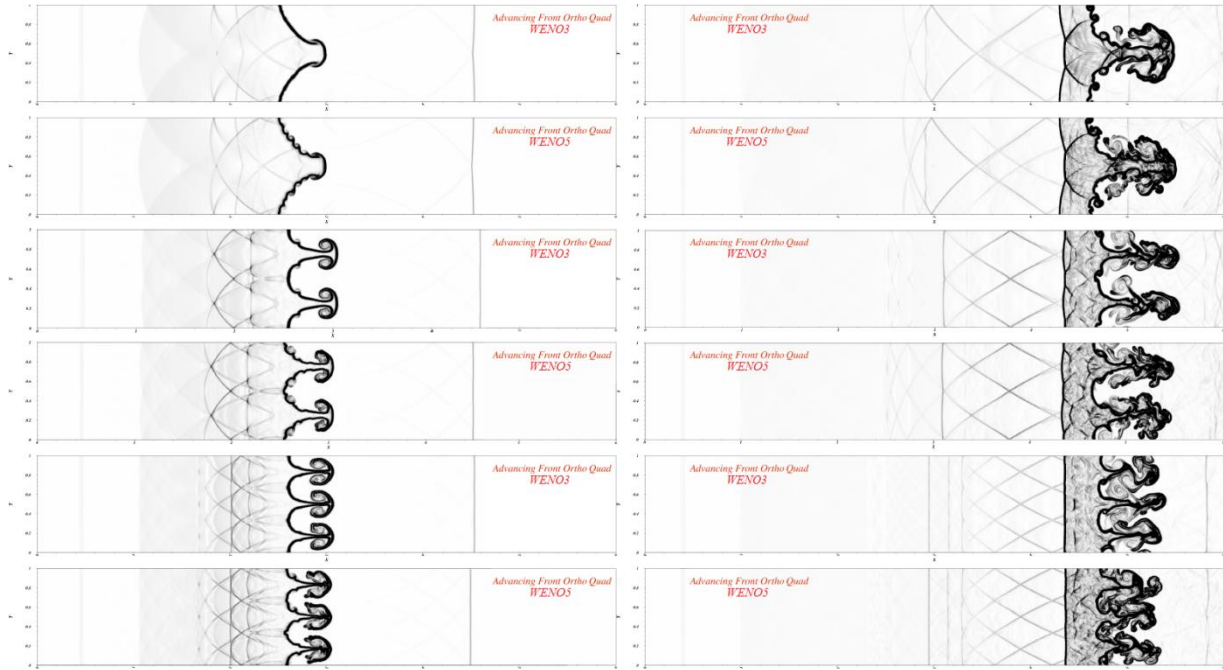


Figure 5. Simulated Schlieren images (density shadowgraphs) for the single, dual, and treble modes of the Richtmyer-Meshkov instability in 2-D at times 1s (left), and 2.25s (right), for the WENO3 and WENO5 schemes. The results are shown for the framework of characteristic variables.

Baroclinic torque accumulates at the sides cap, and shear destabilizes the region. A primitive annular section forms which will evolve in the primary vortex ring, the most distinctive feature of the mushroom. Vortex pairing merges the KH vortices into larger structures. In the end, behind the primary ring, a small, tertiary vortex forms, followed by a larger secondary vortex; in turn the secondary vortex is followed by tertiary ones at the crests of the bubbles. At the very top of the primary vortex for the single mode RMI, the cap develops a kink. This kink develops rapidly with the conserved variables, and it is a point of early symmetry-breaking within their framework without fledging into a vortex. With adequate resolution, it would evolve into a proper tertiary vortical ring for the characteristic variables, akin to those observed for the RTI, whereas for the present resolution it is a dim feature which does not compromise the integrity of the cap. Nevertheless for the multimode instabilities this structure is not detected. For the multimode instabilities, the shear instability disturbs the symmetry of the primary vortex ring which starts to slowly break up into finer and finer structures for the characteristic variables, while the conserved variables deviate from symmetry at much earlier times.

Generally, the results for both the conserved and the characteristic variables are broadly similar, but the conserved variables fail to capture correctly the formation of lesser vortical structures along the stem, and show some discrepancies in the formation of the vortical structures when switching to higher-order schemes. This may indicate a greater sensitivity to the effective numerical Reynolds number. Conversely, a higher-order scheme seems to accelerate the pace of evolution for the vortical

structures. There are also some inconsistencies between conserved and characteristic variables; the latter shows vortices on both sides of the spike, while the former shows a preference for one-sided manifestation of the vortex rings. The final time ( $T = 2.25s$ ) shown in Figure 5 exhibits also the effects of reshock. Impinging the mushroom cap, the wall-reflected shock traverses the spike and perturbs it, which emits a new wrinkled re-transmitted shock. The latter reflects at the wall, straightens and traverses the spike. This process disintegrates the primary vortex ring, and the RMI is triggered along the shattered vortical surfaces, ejecting new mushroom-shaped spikes, which develop rapidly due to compressibility effects, their very small wavelength, and shallow amplitudes. What it is actually observed during and immediately after reshock is memory loss of the fluid flow field, as it gradually enters a self-similar growth regime, where numerical dissipation slowly destroys the smaller scales. This contrasts with the inviscid framework of the Euler equations, and after reshock, the results are deemed non-physical.

### 3. CONCLUSIONS

Unless numerical dissipation can be fully documented, its effects in the solution of any scheme that introduces (always for the framework of the Euler equations) dissipation or dispersion errors cannot be fully regarded as physically meaningful. It is true that smaller dissipations bring the solution closer to the ideal inviscid assumption, however the excessive symmetry-breaking and the fragmentation to smaller and smaller vortical “crumbs” that strive to merge into larger structures even for moderate Atwood numbers needs additional investigation. It possibly hints that the upwinding bias of the stencils will have to be tempered if not even eliminated. Triangular elements introduce the smallest amount of dissipation, and perhaps the most compact stencils form with fully triangular meshes; which algorithm provides better consistency with the optimal stencil is not yet determined, however.

Resolution notwithstanding, for the HLLC framework the results are particularly sensitive to the meshing algorithms. The primary response to discretization increments is symmetry-breaking due to the lower degree of dissipation which permits smaller structures to be resolved. For the more dissipative central scheme of the Rusanov’s flux the results largely retain the symmetry of the flow. Characteristic variables and the  $k^{\text{th}}$ -order WENO schemes of this framework entail the use of the non-linear combination of the  $(k - 1)$ -order reconstruction. The characteristic variables are also responsible for better, more stable vortical representation, being perhaps less susceptible to diffusion.

Results in the literature from structured solvers resemble the behavior of Rusanov’s flux (f.e. primary vortex patterns share many similarities) for low orders of accuracy and quadrilateral elements, hinting that the framework of UCNS3D introduces little dissipation. This corroborates the work of Tsoutsanis et. al. (2015) for the cost-effectiveness of the unstructured framework of the solver, permitting the election of lower polynomial degrees while retaining most of the efficiency of a high-order WENO scheme for structured solvers (f.e. a WENO9 for structured codes corresponds to a WENO7 for unstructured solvers).

To this point, quadrilateral cells appear to require higher order of accuracy to resolve the same structures as the triangular grids. Even if the quadrilateral stencils extend to a greater area than their triangular counterparts due to the non-local reconstruction (hence they might capture more information), the arbitrary orientation of triangular meshes introduces the numerical KHI earlier, and have a smaller degree of dissipation since they have less interfaces, and provide the same if not better resolution.

Loss of symmetry for low resolutions and orders of discretization is attributable to round-off errors, entropy discrepancies, and their amplification by the physical instability. Very high order of accuracy requires low CFL numbers to avoid “ringing” and unacceptable dispersion, unless mesh resolution is high enough. For higher order of accuracy, the non-linear mixing structures become prominent for the HLLC earlier than the Rusanov, which may indicate collaboration between the upwind HLLC and the upwinding bias of the stencils in the WENO schemes. Higher mesh resolutions show also loss of symmetry but the source is the physical instability amplified by the numerical Kelvin-Helmholtz instability, not the truncation errors.

#### 4. REFERENCES

Balsara D., Shu C.-W., “Monotonicity preserving Weighted Essentially non-Oscillatory Schemes with Increasingly high-order of Accuracy”, *Journal of Computational Physics* 160 (2) (2000) pp[405–452].

Kull H.-J., “Theory of the Rayleigh-Taylor Instability”, *Physics Reports* 206 (5) (1991) pp[197–325].

Richtmyer R. D., “Taylor Instability in Shock Acceleration of Compressible Fluids”, *Communications on Pure and Applied Mathematics* 13 (2) (1960) 297–319.

Taylor G.I., “The instability of liquid surfaces when accelerated in a direction perpendicular to their planes. I”, *Proc. R. Soc. London. A* 201 (1065) (1950) pp[192–196].

Tritschler V., Olson B., Lele S., Hickel S., Hu X., Adams N., “On The Richtmyer-Meshkov Instability Evolving from a Deterministic Multimode Planar Interface”, *Journal of Fluid Mechanics* 755 (2014) pp[429–462].

Tsoutsanis P., Kokkinakis I., Könözy L., Drikakis D., Williams R., Youngs D., “Comparison of structured and unstructured-grid, compressible and incompressible methods using the vortex pairing problem”, *Computer Methods in Applied Mechanics and Engineering* 293 (2015) pp[207–231].  
doi:10.1016/j.cma.2015.04.010.

Vorobieff P., Tomkins C., Kumar S., Goodenough C., Mohamed N., Benjamin R., “Secondary Instabilities in Shock-Induced Transition to Turbulence” *WIT Transactions on Engineering Sciences* p.45.

Zhang Y., Shi J., Shu C., Zhou Y., “Numerical viscosity and resolution of high-order weighted essentially nonoscillatory schemes for compressible flows with high reynolds numbers”, *Phys. Rev. E* 68 (2003) 046709.

Zhang Y., Shu C., Zhou Y., “Effects of Shock Waves on Rayleigh-Taylor Instability”, *Physics of Plasmas* 13(6) (2006), 062705.

Zhang P., Wang J., “A Newly Improved WENO Scheme and its Application to the Simulation of Richtmyer-Meshkov Instability”, *Procedia Engineering* 61 (2013) 325–332.

Zhou Y., “Rayleigh-Taylor and Richtmyer-Meshkov Instability Induced Flow, Turbulence, and Mixing. I & II”, *Physics Reports* 720-722 (2017) pp[1–136].